Applied Surface Science Advances 22 (2024) 100622

Contents lists available at ScienceDirect

Applied Surface Science Advances

journal homepage: www.sciencedirect.com/journal/applied-surface-science-advances

Full Length Article

Exploring the impact of laser surface oxidation parameters on surface chemistry and corrosion behaviour of AISI 316L stainless steel

Mark Swayne [a,b,*], Gopinath Perumal [a,b], Dilli Babu Padmanaban [c], Davide Mariotti [d], Dermot Brabazon [a,b]

[a] I-Form Advanced Manufacturing Centre Research, Dublin City University, Glasnevin, Dublin 9, Ireland
[b] EPSRC & SFI Centre for Doctoral Training (CDT) in Advanced Metallic Systems, School of Mechanical & Manufacturing Engineering, Dublin City University, Glasnevin, Dublin 9, Ireland
[c] Plasma Science and Nanoscale Engineering Group, School of Engineering, Ulster University, York Street, County Antrim, Belfast, United Kingdom
[d] University of Strathclyde, Department of Design, Manufacturing & Engineering Management, James Weir Building, Office JW703n, 75 Montrose Street, Glasgow G1 1XJ, United Kingdom

ARTICLE INFO

Keywords:
Laser induced oxidation
Oxide film characterisation
316L Stainless steel

ABSTRACT

This study delves into the corrosion resistance enhancement of stainless steel through laser processing, focusing on the interplay between surface chemistry, morphology, and electrochemical properties. Two sets of 3 × 3 full factorial design of experiment (DoE) designs were employed to explore the influence of laser process parameters, including power, scan speed, frequency, and hatching distance. The findings underscore the superiority of reduced areal energy in producing optimal corrosion resistance 10 times better then unprocessed stainless steel, demonstrating the best results under optimized conditions of a 15 μm hatching distance, 250 mm/s scan speed, 100 kHz frequency, and 80 % power. X-ray Photoelectron Spectroscopy (XPS) analysis reveals the predominant surface composition of iron and chromium oxides, with variations in the oxide combinations correlating closely with areal energy. Depth profiling revealed the transformation of oxide layers and highlights the importance of chromium-to-iron ratio in surface corrosion behaviour. Cyclic polarisation results demonstrate the formation of passive, transpassive, and pitting domains, with metastable pitting observed in some samples. The direct positive correlation recorded between corrosion current and Cr/Fe ratio underscores the significance of oxide composition in corrosion resistance. Electrochemical impedance spectroscopy (EIS) further confirmed the superior corrosion resistance of laser-processed samples to non-laser processed samples, with lower areal energy exhibiting higher resistance compared to higher areal energy. SEM morphology analysis revealed the removal of surface defects and the formation of a protective oxide layer in laser-processed samples, with lower areal energy samples exhibiting the lowest level of surface defects. The 3D optical profilometer measurements of corrosion pits corroborate these findings, with lower areal energy samples demonstrating the lowest pit depth and area, indicating superior corrosion resistance. Overall, this study provides comprehensive insights into optimizing laser processing parameters to enhance the corrosion resistance of stainless steel, offering valuable understanding and strategy for improving the metal surface corrosion resistance.

1. Introduction

Stainless steels especially 316 L have increasingly been used in the pharma and food industries because of its high mechanical strength, good surface gloss, as well as high resistance to both general and localized corrosion. The excellent corrosion resistance originates from the native Cr oxide protective layer on the stainless steel surface, which can act as a barrier against the intrusion of the corrosive media. Therefore, the production of a denser and thicker oxide film with appropriate chemical composition on the stainless steel surface is of importance and significance for further improving their corrosion resistance [1].

In recent years, laser processing techniques have emerged as promising methods for modifying the surface properties of metallic materials, offering precise control over surface characteristics such as roughness, microstructure, and composition [2–4]. These techniques, including

* Corresponding author.
E-mail address: Mark.swayne2@mail.dcu.ie (M. Swayne).

https://doi.org/10.1016/j.apsadv.2024.100622
Received 22 April 2024; Received in revised form 19 June 2024; Accepted 15 July 2024
Available online 23 July 2024

Table 1
Composition of the SS316L sheet material utilised in this work.

Chemical	Fe	C	Cr	Mn	Mo	Ni	N	P	Si	S
Composition (%)	Bal.	0.013	16.6	1.4	2.0	10.0	0.04	0.02	0.425	0.006

laser surface melting, laser surface alloying, and laser surface cladding [5–7], enable tailored modifications that can potentially enhance the corrosion resistance of stainless steel. In this work we look into the effect of altering laser processing parameters on the modification of the native oxide film present through a process called laser induced oxidation.

Laser induced oxidation is an almost instantaneous process due to the rapid heating and cooling of the laser modification this causes a non-equilibrium oxidation process to occur. This highly precise processing method allows for the fine-tuning of the thickness and chemical composition of the oxide film. Cui et al. examined the formation of an oxide film on AISI 304 stainless steel using a 1064 nm Nd:YAG pulsed laser and derived a thermokinetic model to help define the film's composition [8]. This model was used in this work to help define and understand the diffusion of elements. Due to the Gaussian energy distribution the energy decaying radial outwards from a typical laser spot, a non-homogenous composition and morphology often result [9]. The results from this past work show a 2-fold increase in the concentration of Cr on the surface over that of the original sample. The reason for this is due to the relationship between the thermodynamic and kinetic reaction occurring in the process. Initially the formation of Cr_2O_3 oxide is preferred over the formation of Fe_2O_3 as chromium has a lot higher affinity for the chemisorbed oxygen than iron does, so it is thermodynamically favorable. This causes an initial increase of chromium at the surface of the stainless steel, However, due to the higher temperature at the center of the laser spot and the higher diffusion rate of Fe inside the oxide layer, Fe_2O_3 appears on the stainless steel surface. This in turn, produces a duplex oxide at the center of the laser spot [8]. Secondary compounds also become present in the surface layer such as spinel $FeFe_2$-xCrxO_4. These results were consistent with the work done Li et al. and Lu et al. [10,11].

Li et al. used this model to produce a variety of thickness levels of the oxide film on the stainless steel surface by varying the laser power, focal offset and scanning direction [10]. In the study by Lecka et al., the corrosion resistance in 3 % sodium chloride solution and sulphuric acid of the laser induced oxides produced on the AISI 304 stainless steel was investigated [12]. Quite similar results were seen for both the testing environments with an initial large increase in corrosion resistance up to a maximum with a lower fluences of 50 -70 J/cm^2 then a sharp decrease back down to a minimum. These results almost perfectly match the work done by Li et al. and Cui et al. with respect to the chromium to iron ratio produced on the surface [8,10]. At higher fluence, temperature of the surface is increased allowing more time for the diffusion of iron through the oxide layer. This decreases the Cr/Fe ratio on the surface of the metal which in turn decreases the effect of the passivation layer causing a lower corrosion resistance [13]. Zhu et al. investigated the effect of laser processing on the microstructure of 304ss. The laser processing altered the microstructure of the top most surface to be composed of ultrafine grains with dislocation in the sublayer. This grain refinement allowed for the production of a more homogenous oxide layer which increased the pitting resistance of the surface [14].

Laser induced oxide formation and its effect on corrosion properties has been studied for a variety of different materials such as 304 stainless steel and Ti_4Al_4V but there are fewer publications on 316 stainless steel [10,15,16] and much less on The effect of the individual laser processing parameters. To fill this gap in this paper, the effect of altering the laser processing parameters on the laser surface oxidation on 316 L stainless steel and its effect on its corrosion properties have been studies in this work and are presented herein. For the first time in the literature this paper presents the use of long term EIS and depth profiling XPS to elude and compare the long term behaviour of the samples and to identify how the surface and subsurface oxides influence the corrosion results.

2. Materials and methods

SS316L sheets of 1.7 mm thickness were purchased from Impact Ireland (Metals) Limited, Ireland. The composition of the sheet is given in Table 1. Disks of 100 mm diameter was sectioned from the sheet using an industrial CO_2 (CW) laser. All samples were cleaned using deionized water and then ethanol. The surface of the steel was then uniformly sandblasted to increase surface roughness to 3.9 μm Sa to enhance the laser wavelength absorption [2].

2.1. Laser processing

The sand blasted samples were cleaned with acetone, ethanol and sonicated for 15 min to remove any contaminants or excess sand from the surface then allowed to dry for 5 min on the laser stage. The laser system used consisted of a 3.5 W maximum power 1064 nm Q-switched, diode-pumped solid-state neodymium-yttrium aluminium garnet laser (Bright Solutions 1064 WEDGE HF). A 2D scanning galvanometer (Raylase SS-12) was used to raster the beam in the xy-plane, and a movable z-stage (PI M-404 4PD) used to control the position of the sample. The beam was focused on the sample surfaces, which were placed 34.03 mm below the galvanometer lens at the focal plane to produce a spot diameter of 100 μm. Laser areas of 5 mm X 5 mm were processed using fixed parameters of a bidirectional hatching strategy with a hatching distance of 10 μm. Compared to more complicate scanning strategies, a bidirectional hatch strategy provides a more uniformly repeating heat flow during processing.

2.2. Surface characterization analysis

X-ray photoelectron spectroscopy (XPS) was performed on laser processed 316 L SS samples using an ESCALAB Xi+ spectrometer microprobe (Thermo Fisher Scientific) with a focussed monochromatic Al Kα X-ray source ($h\nu$ = 1486.6 eV, spot area of 650 μm x 650 μm) operating at a power of 225 W (15 kV and 15 mA) and the photoelectrons were collected using a 180° double-focusing hemispherical analyser with a dual detector system. The base pressure of analysis chamber was always maintained $< 5 \times 10^{-9}$ mbar, which increased up to $\sim 5 \times 10^{-7}$ mbar during measurement along with charge neutraliser (flood gun) operated at 100 μA emission current. XPS sub-surface chemical composition analysis was performed using a soft cluster clean and monoatomic depth profiling using Ar gas. In the cluster clean, the sample surface of raster size 3.25 mm were exposed to Ar clusters of 1000 atoms, energy at 4 keV for 30 s. XPS depth profiling was performed using 4 keV Ar+ monoatomic beam on a raster area of 1.5 mm on the sample. The sputter rate at 4 keV energy for the sample is referenced to Ta_2O_5 sample (BCR −261T standard) to 0.96 nm/s as given by Avantage operation software. Further relationship between sputter rates of different compounds to standard Ta_2O_5 can be understand from references [17,18]. In all these cases, survey scan spectra were recorded with parameters of step size 1 eV, pass energy 150 eV and narrow core shell high resolutions scans were taken at step size of 0.1 eV, pass energy of 20 eV. Casa XPS software was used to analysis the results for elemental and chemical oxidations states of all elements of interest. The $2p_{3/2}$ peak was taken into account for the composition analysis of chromium, and Iron while for oxygen the 2 s singlet peak was used and for molybdenum both the $3p_{5/2}$ and $3p_{3/2}$ peaks were taken into account. The sensitivity factor and peak position can be seen in Table 3 below.

Table 2
Selected samples and laser process parameters for production of the laser surface oxidised samples.

Sample	Power (W)	Frequency (kHz)	Scan-Speed (mm/s)	Hatching Distance (μm)	Time (s/ m^2)
1 (S1)	1.52	60	50	10	20,000
2 (L24)	2.60	100	450	8	2778
3 (L25)	2.60	100	250	15	2667
4 (L21)	3.44	100	250	10	4000
5 (S27)	2.60	100	450	1	22,222

2.3. Electrochemical corrosion test

For the characterization of corrosion behaviour electrochemical measurements were performed using the Potentiostat (Gamry, interface 1000E) with an open beaker 3 electrode cell with an Ag/AgCl reference electrode, graphite rod counter electrode and the working electrode being the laser processed samples. To isolate the samples, they were first cut into individual pieces using a precision saw. The edges of the samples where then ground using a low grit paper to remove any burs or blemishes. A 3D printed isolation holder was used to just expose the

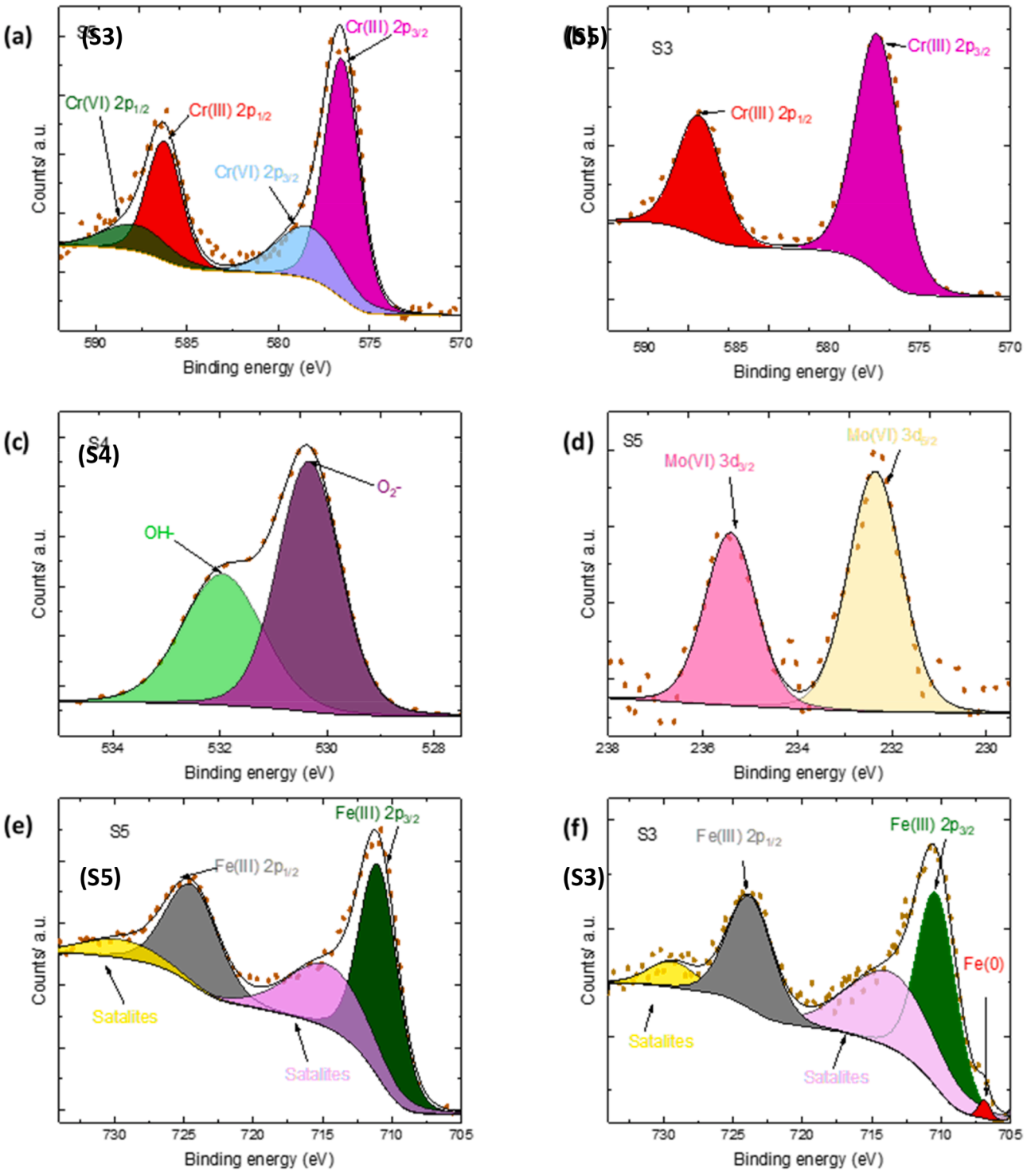

Fig. 1. High resolution XPS spectra of (a) Cr 2p for S3, (b) Cr 2p for S5, (c) O1s spectra of S4, (d) Mo 3d of S5, (e) Fe 2p for S5, (f) Fe 2p of S3.

Table 3
Binding energies and sensitivity of the compounds used in this study [20–22].

Peaks	Compounds	Binding Energies (eV)		Sensitivity Factor
		Experimental	Reference	
Fe 2p 3/2	Fe (metal)	706.8	706.5	
	Fe_2O_3	710.9	710.8	10.82
Cr 2p 3/2	Cr (metal)	574.8	574.3	
	CrO_3	580	580	7.69
	Cr_2O_3	577	576	7.69
O 1s	O_2 -	530.1	529–530	2.93
	OH-	532.0	531.5–532	
Mo 3d 5/2	MoO_3	231.5	232	5.62
Mo 3d 3/2	MoO_3	236.1	235.6	3.88

surface. An open circuit potential (OCP) was first carried out on the sample in 0.5 M NaCl for 10,800 s to obtain the OCP. Electrochemical impendence spectroscopy (EIS) was then carried out with Impedance data collected at OCP over a frequency range from 10 mHz to 10 MHz with peak to peak amplitude of 10 mV. Circuit models were designed using Gamry Echem analyst software. A second OCP was then measured for 3600 s to act as a reference point for the cyclic polarization (CP). Cyclic polarization was then preformed on the sample with a forward scan rate of 0.1667 mV/s between -0.3 V to 1.5 V against the OCP. Once the maximum voltage was achieved the reverse scan started with a scan rate of 0.1667 mV/s down to -0.3 mV/s of the OCP. Tafel plot interpolation was used to extract the corrosion data for the cyclic polarization curve.

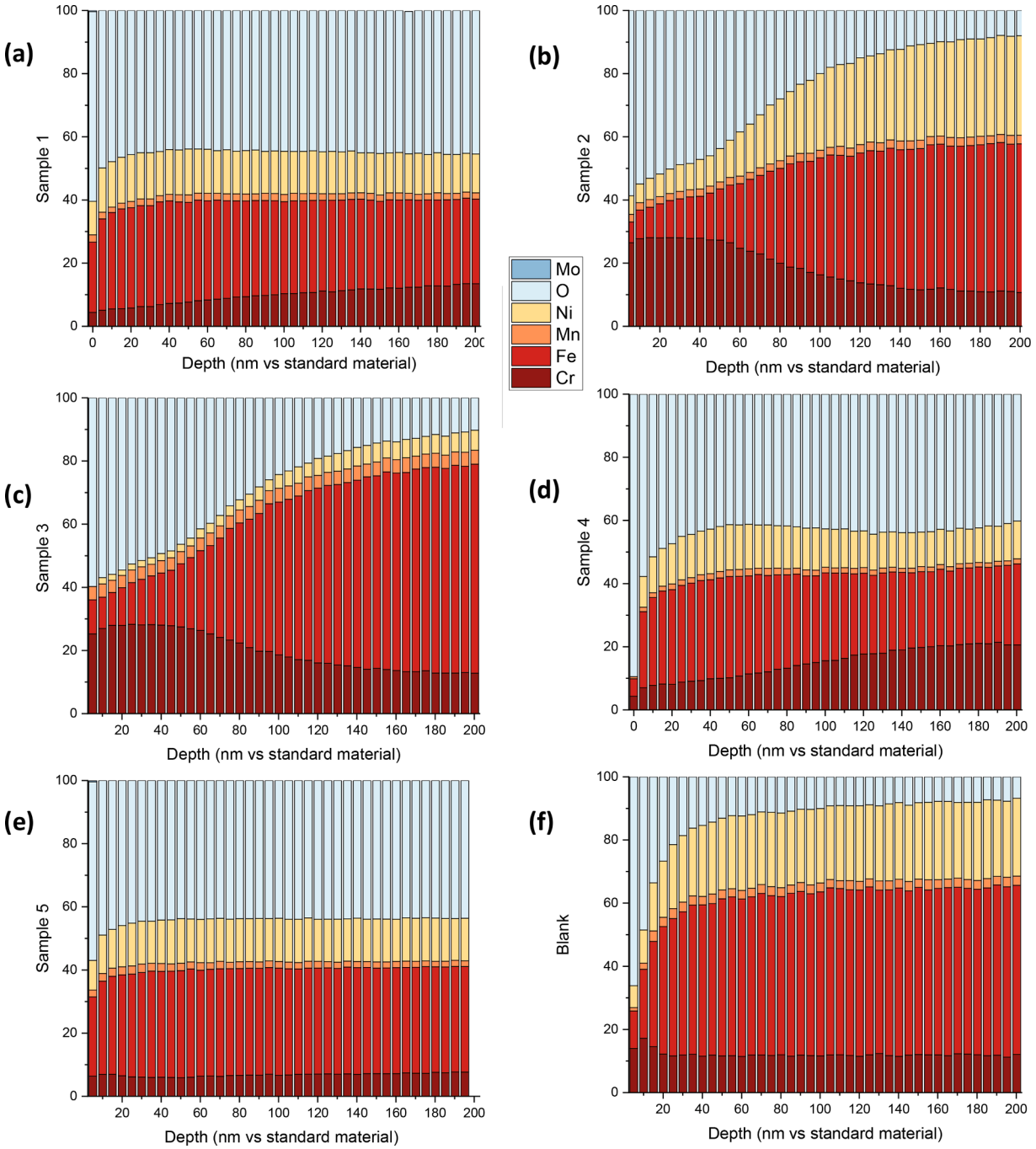

Fig. 2. XPS depth profile of laser-processed vs Ta_2O_5 standard material (a) S1, (b) S2, (c) S3, (d) S4, (e) S5, and (f) blank sample.

Table 4
Surface composition of the laser processed samples, including the Cr/Fe ratio and the oxide layer depth.

Sample	Fe (at%)	Cr (at%)	Mn (at%)	Ni (at%)	Mo (at%)	O (at%)	Cr/Fe	Oxide Depth
Sample 1	23.38	4.33	1.92	12.00	0.34	58.03	0.19	>200
Sample 2	6.01	21.67	3.04	4.75	0.00	64.52	3.61	75
Sample 3	9.24	21.17	4.38	0.00	0.00	65.21	2.63	85
Sample 4	7.33	5.90	0.22	0.00	0.00	86.55	0.80	25
Sample 5	23.12	5.85	2.29	9.79	0.32	58.63	0.25	>200
Blank	14.01	9.92	0.61	6.37	0.00	69.09	0.71	15

2.4. Morphology analysis

Optical imaging was performed using a VHX-2000 (Keyence) 3D optical microscope. Scanning electron microscopy was conducted using JSM-IT 100 (Jeol).

3. Results

Two distinct full factorial design of experiment (DoE) designs (3 × 3) were conducted to examine the effect of the laser process parameters. The process factors examined in the first model were laser power (W), scan speed (mm/s), and laser frequency (kHz). The processing factors and their levels examined are listed in supplementary information. The optimal values of the laser frequency (100 kHz) from the first DoE were used in the second model. The findings from the first DoE showed that reduced areal energy produced superior corrosion results, so the scan speed and laser power were also investigated in the second DoE. To further investigate the effect of laser processing on the corrosion, five samples were selected from the two DOEs with varying corrosion results the samples and parameter can be seen in Table 2

To be able to normalize the process parameters into a single parameter, the areal energy equation was calculated. It takes into account the total number of laser impacts, the laser fluence of an individual pulse, and the pulse overlap with the Pulse fluence being defined as the laser power divided by the laser spot area and d being the spot size area:

$$Areal\ energy = \frac{Pulse\ Fluence}{(d^2 * (1 - Hatching\ overlap)(1 - Pulse\ overlap))} \quad (1)$$

3.1. Surface concentration

X-ray Photoelectron Spectroscopy (XPS) was conducted on the five laser-processed samples to analyse the surface chemistry of four key compounds: iron, chromium, oxygen, and molybdenum. Casa XPS software was initially used to determine the relative concentrations of these compounds by measuring the ratio of peak areas. Notably high peak intensities of iron, oxygen, and chromium were observed in all samples, suggesting a predominant surface composition of iron and chromium oxides. For detailed analysis, refer to the high-resolution XPS data in Fig. 1 and Table 3 provides information on sensitivity factors, reference peaks, and experimentally recorded peak positions.

Fe 2p Spectra (Fig. 1 e-f): Examining the Fe 2p spectra reveals the presence of four prominent peaks at binding energy values of 710–711 eV, 724–725 eV, 715–716 eV, and 729 eV, corresponding to Fe $2p_{3/2}$ and Fe $2p_{½}$. Notably, the peaks at 716 eV and 729 eV are identified as satellite peaks, indicative of Fe (III) oxides, specifically Fe_2O_3. In the case of lower areal energy runs, such as S3, an additional peak at ~706 eV is observed, signifying incomplete oxidation and the presence of metallic Fe on the surface. O1s Spectra (Fig. 1 c): For all runs, the shape of the O1s peak was very similar. This peak forms at binding energy 530.4 eV and with a full width half max (FWHM) of 1.5 eV indicating an O_{2-} metal oxide; this indicates that the laser processing has oxidized the steel surface. Shoulder peaks are also present with a binding energy of 532.1 eV due to the presence of OH- in part due to metal hydroxides. The O_{2-} / OH- ratio in the oxide film was calculated from the O 1 s spectra, with a larger variation in ratios throughout the processed samples with S3 having an O_{2-} / OH- ratio of 8.01 and with S4 having a ratio of 1.11. These both show higher oxide ratios than the unprocessed sandblasted sample at a ratio of 0.61. This ratio plays an important role in the pitting corrosion as hydroxides film are more defect prone than oxide film so this increase in the ratio can positively impact the density of the passive film present on the steel surface [19]. The amount of oxygen present on the surface is a lot higher in S4, which is explained by the higher content of hydroxides present compared to the other processed samples. Mo 3d Spectra (Fig. 1d): The Mo3d spectra displayed two major peaks at binding energies of 232.36 eV and 235.42 eV, corresponding to Mo^{6+} $3d_{5/2}$. The concentration of Mo is only detectable in samples 1 and 5, due to the higher power used allowing longer diffusion times, but the concentration is still extremely low at under 1 %. Cr 2p Spectra (Fig. 1 a-b): The Cr 2p spectra reveal three primary peaks at binding energies around 577 eV, 580 eV and 587 eV, corresponding to Cr $2p_{3/2}$ for Cr(iii) oxide, Cr $2p_{3/2}$ for Cr(vi) oxide, and $Cr_{½}$ for both oxides, respectively. The identified oxides include Cr_2O_3 and CrO_3. Analysis discloses the formation of three distinct oxide combinations on the laser-processed surface: Notably, these oxide combinations closely correlate with areal energy, with lower areal energy in S3 favouring Cr_2O_3 with 100 % of the Cr(iii) peak against 0 % of CrO_3. In contrast, higher areal energy in S5 favours CrO_3, with the Cr(vi) peak at 89% vs. 11 % of the Cr(iii) peaks corresponding to Cr_2O_3.

3.2. Depth profile

Fig. 2 shows the XPS depth profiles of the five selected laser processed samples (See Table 2) and the unprocessed blank samples. These profiles show that the individual elements vary quite drastically through the depth of the oxide layer; the oxygen content of the laser processed samples is elevated compared to the blank samples further into the depth profile showing an expansion of the oxide layer. An interesting observation is the variation in nickel content between samples 2 and 3 where the chromium content varies similarly throughout the profile but S2 has an increase in nickel content further into the profile while S3 has an increase in Fe. All other samples have a relatively constant oxide layer composition after 20–40 nm vs Ta_2O_5 into the depth profile, while samples 2 and 3 vary throughout the entire profile. The oxide layer thickness was measured using a O 50 % method, where the concentration of the oxygen drops below 50% of its original value [23,24]. Table 4 shows the results, samples 1 and 5, have a very larger oxide layer present greater than the depth profiled. Samples 2 and 3 show similar oxide behaviour at values in the 75–85 nm range, samples 4 and the blank also show similar results.

The analysis of Mo into the depth profile was hindered due to the argon etchant used which can cause the Mo oxide to be reduced to a mixture of lower oxide states and can cause them to not be detected at the low concentrations.

Examining the variation in the Cr/Fe ratio throughout the depth profile provides insights into the transformation of oxide layers. The blank sample exhibits a consistent decrease in the Cr/Fe ratio up to 20 nm, levelling off into the bulk stainless steel, indicating the presence of a single-layer oxide. Samples 4 had a similar Cr/Fe ratio starting behaviour as the blank sample but this started to increase further into the

depth profile. This shows that it had a thin outer passive layer but a larger oxide layer depth in total compared to other samples.

Samples 1 and 5 show similar behaviour with an almost constant Cr/Fe ratio throughout the entire depth profile, with a ratio very similar to that of bulk stainless steel. This shows that for the higher areal energy runs the protective passive layer seems to almost be fully removed after processing.

S2 shows the highest initial Cr/Fe ratio, being over 4.0. The ratio sharply drops over the first few nm. Where it meets a turning point in the results, these inflection points could be indicative of a multilayer oxide forming on the surface, which has been seen previously in the literature (references). S2 has two discrete turning points one at 5 nm and one at 35 nm.

S3 shows a slightly different behaviour to the rest if the oxides where the Cr/Fe ratio increase over the initial few nm of the passive film going from 2.3 to 2.6 over the first 5 nm showing that there is a chromium enriched inner oxide layer. It meets an inflection point and starts to decrease in value again. This indicates that the lower areal energy does not allow for full diffusion causing a smaller altered layer thickness.

3.3. Cyclic polarisation results

Fig. 4 depicts the potentiodynamic polarization curves of 316 L stainless steel with the five varying laser-processing conditions in a 0.5 M NaCl solution at room temperature. As increasing polarization potentials, the curves of all steels contain the active, passive, transpassive and oxygen evolution process regions. The first passive domain is associated with the presence of a chromium oxide based passive layer. The magnitude and occurrence of this layer is driven by the oxidation processing and is therefore directly related to the chemical composition of the passive oxide layer.

When the electrical potential exceeds a critical threshold, chloride ions migrate toward the interface between the metal and oxide layers, resulting in the creation of a metal chloride phase. This phase cracks the overlying oxide because of its large specific volume. Consequently, the chloride phase becomes a readily available source of chloride ions that foster the initiation and stabilization of pit growth. After pitting nucleation, these pits continue to expand, forming microscale cavities before eventually undergoing repassivation. This ongoing cycle of breaking down and restoring the thin passive film is termed metastable pitting and is a crucial stage. Only the pits that survive this stage have the potential to develop into stable, growing pits [25]. The presence of this metastable pitting phenomenon can be observed in samples 2 and 4.

Ultimately, the dynamic balance between the rupture and repair of the passive film at local defects is disrupted, leading to the formation of stable pits, which is known as the pitting resistance for the given sample. Within these pits, those in a locally activated state (characterized by low potential) serve as the anode, while the majority of the surrounding surface remains passivated (exhibiting high potential) and serves as the cathode. Consequently, an electrochemical corrosion cell with an "big cathode and small anode" is established both inside and outside the pit [26,27]. As the anodic reaction progresses, the concentration of metal cations, such as Fe^{2+}, within the pit increases. To maintain charge neutrality within the pit and balance the charge associated with these cations, chloride anions electro-migrate into the pit. Cation hydrolysis and the absence of a localized cathodic reaction contribute to a decrease in pH within the pits. Once an acidic chloride-rich environment is established within the pits, it facilitates pit growth through an autocatalytic pitting mechanism.

It can also be seen that in samples 1, 4 and 5 that a second zone of repassivation has occurred after the pitting resistance has been surpassed. This is evident by the increase in anodic current density at potential above the pitting resistance. These samples are all associated with a smaller first passive domain than samples 2 and 3, this second repassified layer can be associated with the change of oxidation state of chromium due to the applied electrochemical potential, referred to as Cr transpassivation. This causes a thickening of the surface film and causes a depletion in the Cr content in the oxide due to rapid dissolution of chromium in this domain, making the layer more susceptible to further electrochemical breakdown [28]. This does not occur in samples 2 and 3 due to there more favourable passive layer that does not break down until above the second passive domain of +0.4 V vs SHE.

Table 5
Electrochemical parameters of corrosion current, corrosion potential and pitting resistance ($E_{corr} - E_{pit}$) measured for laser processed samples.

Sample	S1	S2	S3	S4	S5	Blank
Icorr (nA/cm^2)	730.40	49.53	51.50	69.65	301.75	502.00
Ecorr ($mV_{Ag/AgCl}$)	-87.22	-60.30	-66.50	-70.75	-170.00	-125.00
E_{corr}- E_{pit} ($mV_{Ag/AgCl}$)	133.50	395.90	509.15	168.28	105.39	160.80

To further assess the effect of laser processing on the corrosion resistance of the samples, the key electrochemical parameters, namely the pitting resistance, free corrosion potential (Ecorr) and free corrosion current density (Icorr), are determined using the Tafel extrapolation method [29]. Table 5 lists these electrochemical values for all samples.

It can be seen that the Ecorr trends to more noble values with a decrease in the applied areal energy, this higher Ecorr value corresponds to a more compact and protective passive film, being less susceptible to corrosion attack. The two noblest Ecorr values correspond to samples 2 and 3 at -60.3 and -66.5 mV respectfully with the Ecorr value dropping exponentially with an increase areal energy until it reaches the lowest value of -170 mV for S5. This shows that S5 has the least compact passive film, which is evident by the cracks and defects in its passive film.

The pitting resistance ($E_{corr} - E_{pit}$) can also be seen to follow a similar trend where the lower the applied areal energy corresponds to the higher pitting resistance with S3 having the highest pitting resistance at 509.15 mV which is 8 fold increase compared to the unprocessed value of 60.9 mV. It is also seen in Fig. 4 (c) that the corrosion current followed closely the Cr/Fe ratio with a sharp drop off once the Fe content surpasses the Cr in the passive oxide layer, increasing from 49.5 nA/cm^2 to 730.4 nA/cm^2 with an increase in Cr/Fe ratio of 0.179 to 3.61.

These results show that the composition has a strong influence over the general corrosion of the surface while the surface morphology has more of an influence over the localised corrosion. Lower hatching distances result in an increased amount of heating and cooling cycles and thermal stresses inside the layer allowing for more surface defects to be present.

3.4. Electrochemical impedance spectroscopy

EIS test is a common method for evaluating the properties of the passive film on stainless steel surfaces. The Bode and Nyquist plots measured in 0.5 M NaCl solution at OCP of S2,5 and unprocessed are seen in Fig. 5 As the passive film on stainless steel is not always perfectly stable, and its resistance can change with time and exposure conditions. Therefore, the Rp value measured at a specific point in time may not represent the long-term stability of the passive film for this reason we have preformed a long exposure examination with EIS measurement taken over a 10 day period under the same conditions as above. The Nyquist plots of the three samples over the 10-day period are shown in Fig. 6.

The impedance was significantly higher for S2 compared to the unprocessed samples with S5 being significantly smaller then both Fig. 5. The phase angle vs frequency plots for all samples in Fig. 5.show a broad peak in the mid-frequency range which is indicative of the capacitive characteristic of the system. The capacitive characteristic is the result of charge transfer and formation of double layer capacitance at metal/electrolyte interface where, the diameter of the capacitive loop indicates the charge transfer resistance (Rp). Higher Rp signifies lower dissolution

Table 6
Electrochemical impedance spectroscopy results for samples 2, 5 and unprocessed.

Sample	Rtotal (k ohm/cm)	Rp	Cdl (μS s^a/cm^2)	Ru	Ri	CPEi	Ro	CPEo	Rpore	CPEpore
Blank	384,736	375,800	757.5	11.18	8936	5475	–	–	–	–
Sample 2	586,015	547,200	473.4	15.61	15	3592	38,800	773.2	–	–
Sample 5	37,362.85	7639	3599	19.68	6.75	2604	417.1	4355	29,300	1337

rate and correspondingly higher corrosion resistance.

The Nyquist plot for the S2 showed the largest radius signifying highest corrosion resistance amongst all samples. The Bode plot for each of the three samples are unique and show different surface properties, with all samples having multiple time constants. The unprocessed sample is fitted with a circuit with two time constant connected in series; this is due to the oxide layer acting as one time constant and the sand-blasted surface roughness acting as the other. S2 then expands the equivalent circuit to include a third time constant due to the formation of a multilayer oxide being produced. Samples 5 has the same three-time constants in series but also include a fourth time constant in parallel to incorporate the effect of the porosity/cracked outer passive film produced. Therefore, a two-time-constant EEC for the as-received alloy and a three and four-time-constant EEC for both the processed specimens 2 and 5 respectfully were used to model the electrochemical system. The EEC for as-received steel and both the processed specimens are shown as insets in Fig. 8(c) and (d) respectively.

Here, Ru is the solution or electrolyte resistance, Cdl and Rp are the electrochemical double layer capacitance and charge transfer resistance, respectively, for the high frequency part of the spectrum, whereas CPEi and Ri are the corresponding elements inner oxide layer properties. With CPEo and Ro resenting the outer oxide layer and CPEpore and Rpore representing the pore capacitance and resistance. CPE, a frequency dependent constant phase element with exponent α, was used instead of pure capacitance to account for surface in-homogeneities, such as roughness, adsorption, and diffusion. The values of different elements of the electrochemical equivalent circuit are summarized in Table 6 with the more detailed results seen in supplementary information 3.

Rtotal gives the total resistance for the processed and unprocessed specimen (Table 6). The total resistance was found to be highest for S2 followed by unprocessed and then S5. Charge transfer resistance shown by S2 was noticeably higher compared to other two specimens. This is in line with Tafel results, supporting highest corrosion resistance for S2 followed by unprocessed and them S5. In addition, the α value for both the processed samples was higher, indicating better homogeneity of the passive layer. The likely cause of superior pitting corrosion behaviour of processed samples.

Fig. 6 shows the time dependent EIS profiles for samples 2, 5 and Blank, The EIS results all show multiple time constants and the equivalent circuit alters over time, showing a variation in the RP values and EEC. The Nyquist plots of all the samples display a similar semicircle feature under different condition, but at different diameters.

During S5 initial experiences of exposure, a CPE+2 pore equivalent electrical circuit (EEC) develops due to imperfections in the passive film. In the early stages of exposure, the metal surface undergoes passivation, as evidenced by an enlargement of the semicircle feature in the Nyquist plot, see Fig. 6. This results in the formation of a passive film that contributes to the increase in Rp, reflecting the resistance to corrosion. The initial rise in Rp is linked to the growth and stabilization of the passive film. As the passive film thickens and becomes more protective, Rp continues to increase, transforming the EEC into a CPE+2 configuration. This change is indicative of the evolving electrochemical behaviour as the metal surface interacts with its environment. The enhanced Rp signifies a more robust protective layer, indicating the progression of passivation. The impedance steadily rises until reaching a peak on day 4, after which it starts to decline. This decline is attributed to the degradation of the passive film, signifying reduced protection and heightened susceptibility to corrosion. By day 6, localized corrosion initiates, leading to a transition in the EEC to CPE+2, with pores now forming due to pitting corrosion of the passive film. This shift in the electrochemical response is a critical point, highlighting the initiation of a corrosive process that compromises the integrity of the passive film. The formation of pores introduces new pathways for corrosive agents, further accelerating the corrosion process. The overall resistance (Rtotal) continues to decrease throughout the remaining 4-day period, indicating an ongoing deterioration of the metal's corrosion resistance. The detailed understanding of these electrochemical changes can inform strategies for corrosion prevention and mitigation in practical applications.

S2 exhibits distinct mechanistic effects compared to S5. Initially, S2 starts with an EEC of a CPE+2, a configuration that remains consistent as the surface undergoes passivation processes, leading to an increase in impedance. This impedance steadily rises until day 2, reaching its peak, after which it stabilizes, indicating the establishment of steady-state conditions as the passive film attains a stable state.

Rp, representing the passive film resistance, reaches a plateau during this period, suggesting the formation of a relatively constant and well-developed passive film. Over the subsequent 8 days, there were minor fluctuations in impedance, followed by prompt re-establishment of the passive film. These fluctuations may indicate evidence of metastable pitting occurring during electrochemical impedance spectroscopy (EIS) [30].

On day 7, the EEC undergoes a transition, increasing the number of time constants to CPE+3. This change signifies the formation of a multilayer oxide, indicating a complex evolution of the passive film structure. This shift in the EEC configuration provides insights into the ongoing processes of oxide layer formation and the dynamic nature of corrosion resistance mechanisms within S2.

In S3, additional information from the supplementary data 4 reveals an intriguing pattern in the total resistance. Initially, there is a gradual increase in total resistance over the first four runs. However, from runs five to ten, there is a notable and abrupt decrease in resistance. Followed by a sudden and substantial increase where it stabilizes. This fluctuation in resistance dynamics may be linked to the formation of a multilayer oxide. As evident from the depth profile the outer oxide layer formed contains lower chromium content. However, as this outer layer undergoes breakdown, the underlying layer with higher chromium content becomes exposed, leading to an enhanced passivation effect.

3.5. Morphology analysis

SEM images of the laser processed samples 2, 5 and unprocessed are seen in Fig. 7. These two samples experience the lowest and highest areal energy between them. It is evident from Fig. 7 b that the laser processing removes many of the surface defects due to the process of oxide growth and laser remelting and solidification. The oxide growth causes a change in the optical properties of the surface changing the colour of the surface due to the process of thin film interference caused by the production of a thin film oxide. It can be seen for the higher areal energy processed samples (Fig. 7a) that defects start to occur in the oxide film with oxide cracks and a very porous oxide film being produced.

Scanning electron microscope (SEM) image of the corroded surfaces for all cases are shown in Fig. 8. Both unprocessed and S5 showed extensive corrosion, in contrast S2 showed lower overall corrosion supporting its superior corrosion resistance. It was seen that samples 5 experienced a variety of difference corrosion fails; the surface oxide colour was fully stripped which a few very large pits formed, while also

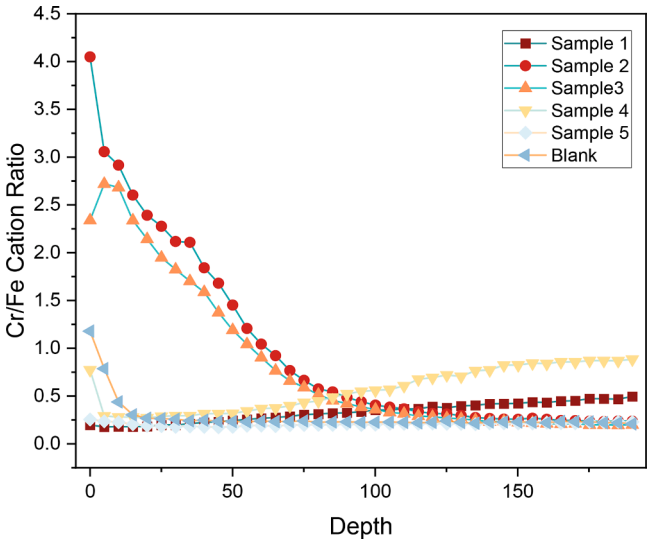

Fig. 3. Cr/Fe ratio throughout the depth profile for all tested samples.

experienced delamination of the oxide layer showing that the oxide is not strongly bonded to the substrate. The unprocessed sample experienced a higher pitting density with multiple larger pits on the surface with no evidence of delamination. S2 seem to perform the best with sight evidence of general corrosion seen by the discolouration of the oxide film at certain location, with only a singular pits present. The 3D optical profilometer measurements of the corrosion pits for all samples are shown in Fig. 8. The pit depth for the unprocessed samples shows a peak at 116 μm compared to the 61 μm for the optimised S2, S5 preformed the worst producing the largest and deepest pits with a peak depth of 354 μm and a pit area six times larger than unprocessed stainless steel. As the surface roughness was quite high in all samples, the peaks could mask the smaller pits and trough the pit density was quite low with larger spacing between each pit, this shows that the area surrounding each large pit became cathodically activated reducing it susceptible to pit initiation.

4. Discussion

The corrosion resistance of stainless steel is mainly attributed to the protective nature of the passive film and its self repairing ability [1,31], a three layer model has been suggested for the passive films on austenitic stainless steel [32,33]. The outmost layer has been shown to composed of a hydroxide film with an oxide layer beneath, this oxyhydroxy film, mainly enriched with Cr(III), is formed on top of a Ni(0) enriched layer in the metallic alloy region. This orientation of the oxide film is clearly seen from the depth profile Fig. 3 (e). During laser irradiation, the outer layer of the oxide film absorbs light through inverse Bremsstrahlung absorption. The absorbed energy propagates into the subsurface atoms exciting the electrons to higher energy levels and become more energetic. In addition, the surface-adsorbed oxygen molecules have a higher probability of decomposing into oxygen ions [34]. Thus, this regeneration of the Mott potential facilitates the continued growth of the oxide layer [35]. The rapid heating and cooling caused by the laser processing

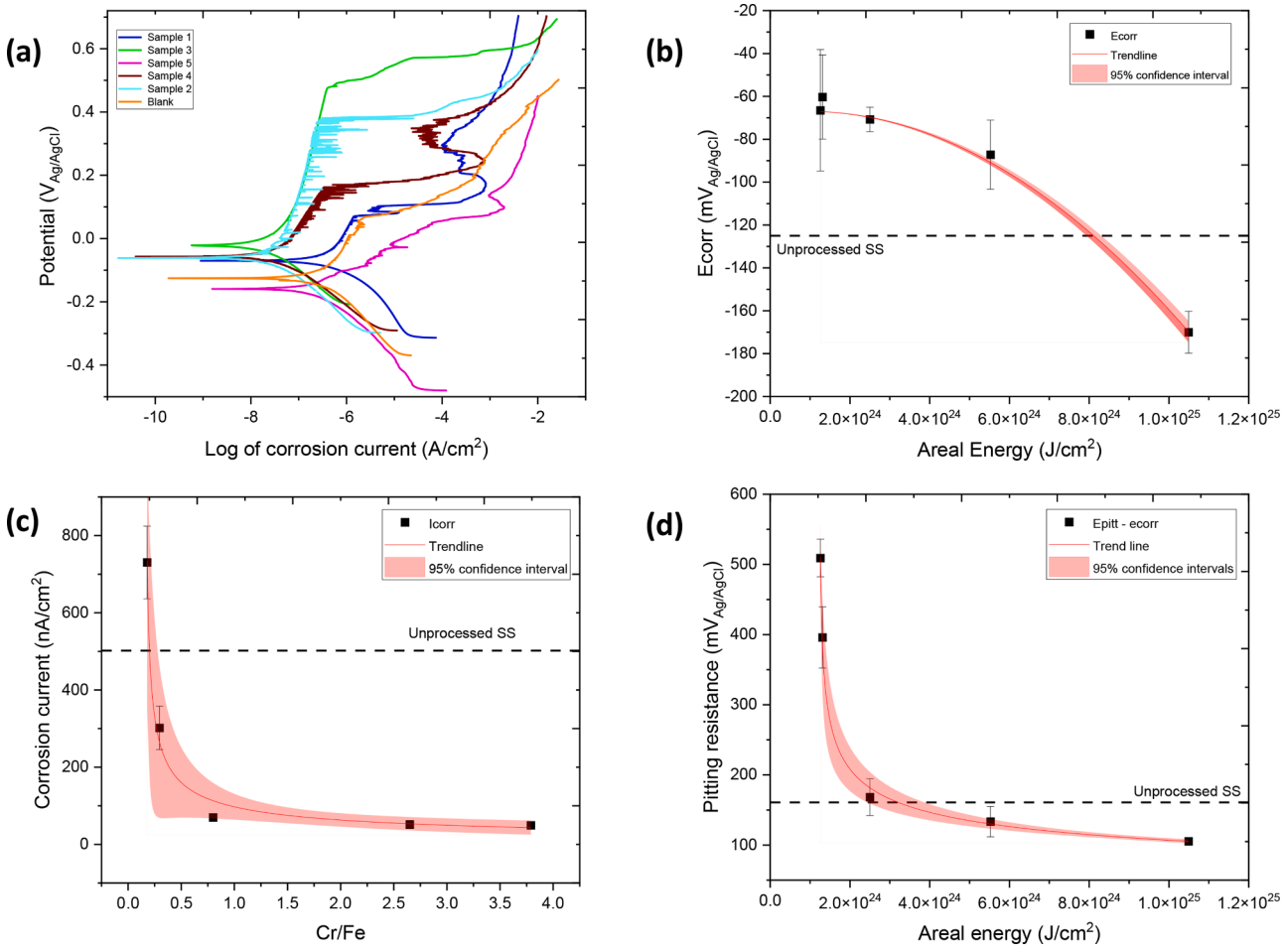

Fig. 4. (a) Cyclic polarization graph of the 5 laser processed samples vs Ag/AgCl, (b) Ecorr vs areal energy, (c) Corrosion current vs Cr/Fe ratio, (d) Pitting resistance vs areal energy.

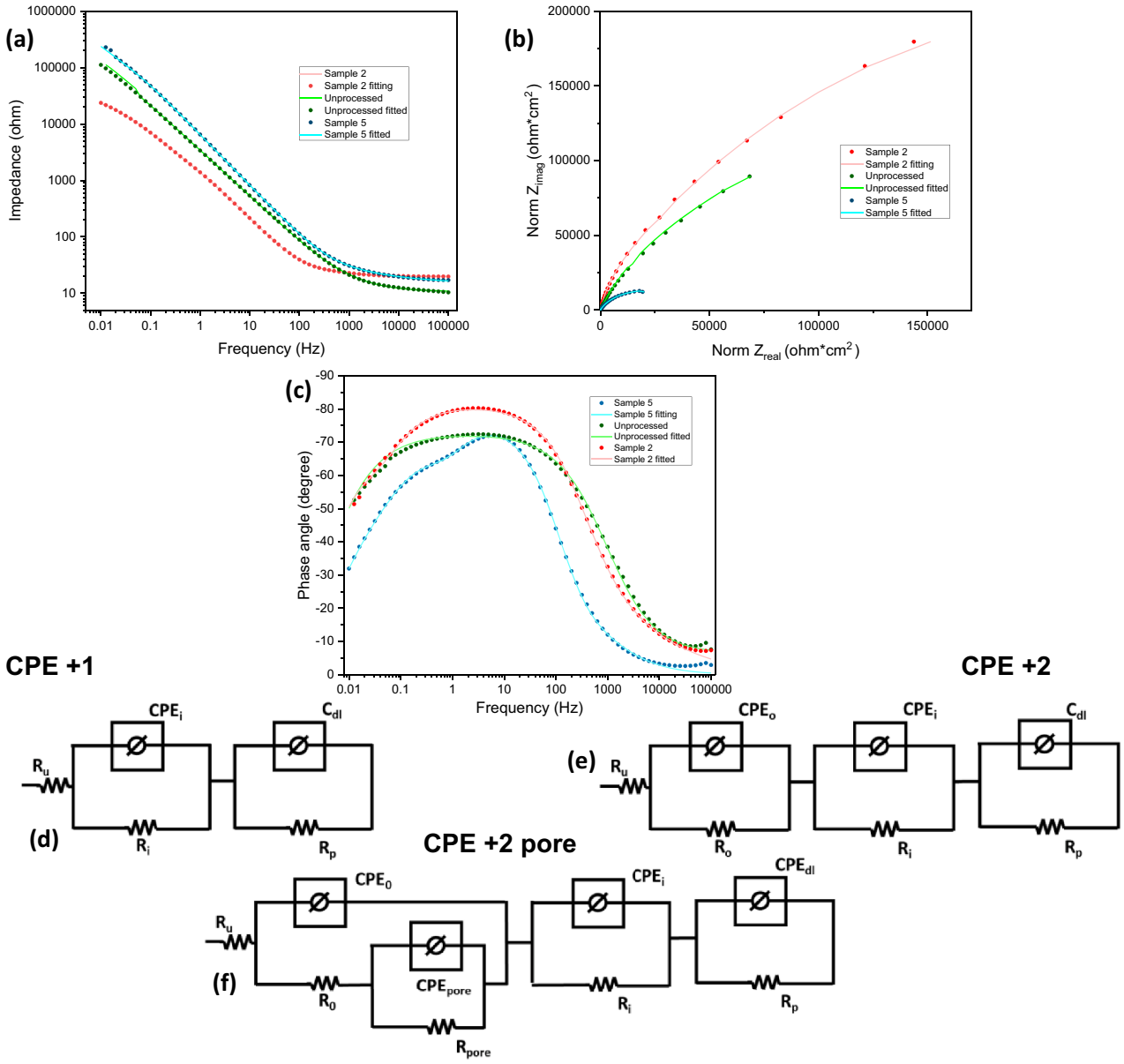

Fig. 5. Electrochemical impedance plots for laser processed samples (a) Bode impedance plot (b) Bode phase plot, (c) Nyquist plot, (d) EEC for Blank (CPE + 1), (e) EEC for S2 (CPE + 2), and (f) EEC for S5 (CPE + 2 pore).

allows for non-equilibrium oxidation of the surface, this gives the ability to fine-tune the oxide composition, which can heavily influence the corrosion properties of the surface.

The optimized laser processed sample was obtained by the ns-laser processing with S3 conditions of a 250 mm/s scan speed, 15 μm hatching distance, 100 kHz frequency and a 80 % power. These conditions led to a peak pitting resistance of 509.15 mV vs Ag/AgCl and an Icorr value of 51.5 nA/cm^2. This shows that the optimal sample (S3) had a corrosion resistance 10 times better then unprocessed stainless steel,

As depicted in Fig. 4, the corrosion current closely correlates with the Cr/Fe ratio observed on the surfaces of laser processed samples, indicating that higher Cr/Fe ratios above 1.0 are associated with lower corrosion currents, indicative of a reduced corrosion rate. This observation highlights the significant influence of the chromium-to-iron ratio on the corrosion behaviour of the samples. Interestingly, the trend of increasing Cr/Fe ratio being more proficient at lower areal energies is noteworthy. For instance, S3 demonstrates a notable Cr/Fe ratio of 3.61 at the lowest areal energy level, suggesting a robust resistance to corrosion. Conversely, S1 exhibits the highest corrosion current despite its longer processing time, which is intriguing considering its relatively low Cr/Fe ratio of only 0.19. This discrepancy highlights the intricate interaction between processing parameters and resulting surface characteristics on corrosion resistance.

Furthermore, the variation in Cr/Fe ratio observed across samples can be explained by the thermokinetic model proposed by Cui et al. [8]. According to this model, at lower areal energies, chromium oxide is preferentially oxidized first due to its higher affinity for oxygen. This initial oxidation results in the formation of a chromium oxide layer on the surface. Subsequently, as more energy is supplied, iron oxide formation occurs. This phenomenon is attributed to the higher mobility of iron ions through the oxide layer compared to chromium ions, leading to the formation of iron oxide over the chromium oxide layer.

The pitting resistance results closely track the areal energy utilized for each sample produced. Notably, S3 exhibits a higher pitting resistance than S2 despite having a lower Cr/Fe ratio. This discrepancy in pitting resistance values, despite similar applied areal energies, can be

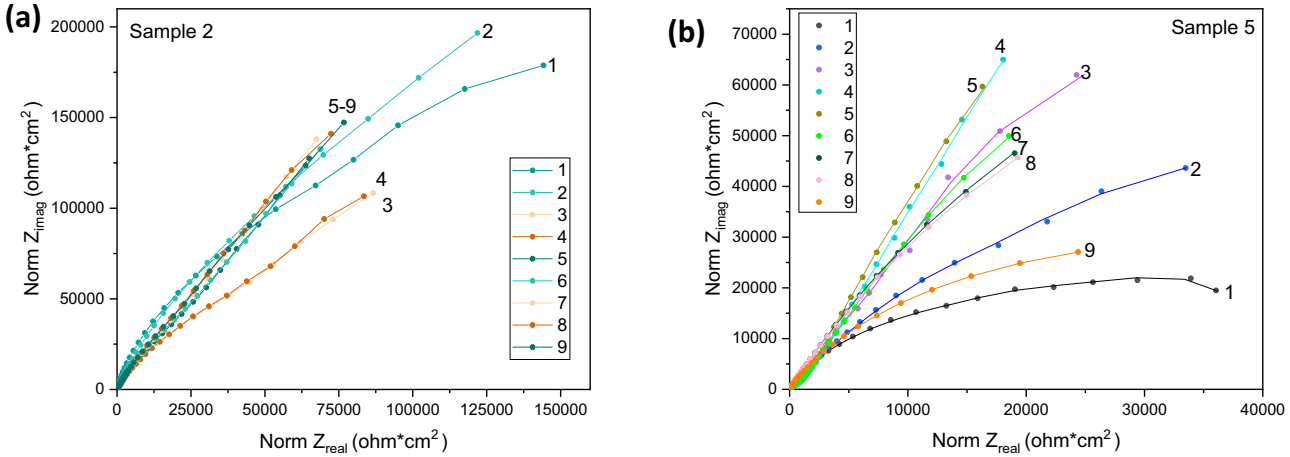

Fig. 6. Long-term electrochemical impedance spectroscopy for laser processed samples (a) S2, (b) S5.

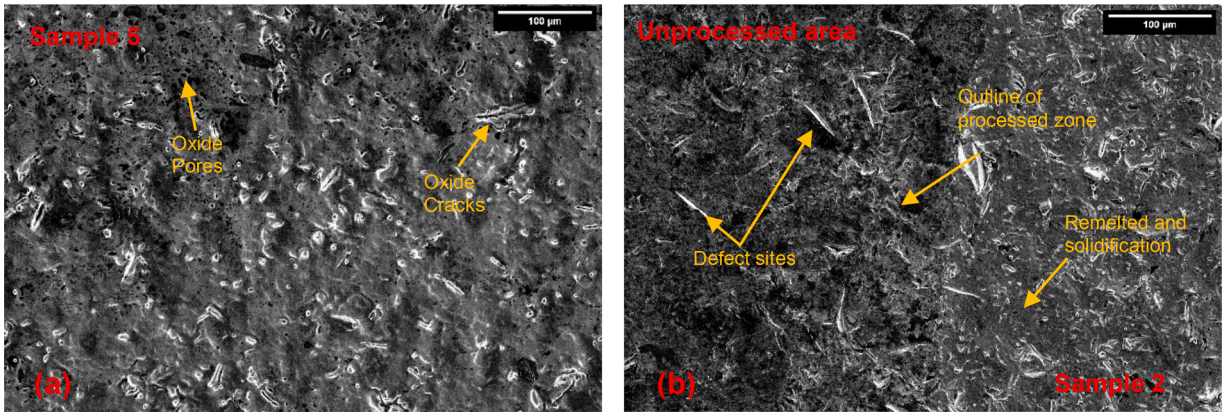

Fig. 7. SEM images of (a) S5 and (b) S2 and unprocessed sample.

elucidated by the increased hatching distance employed in producing S2. It is conceivable that the reduced laser overlap at greater hatching distances contributes to enhanced pitting resistance. This reduction potentially mitigates the thermal stress within the oxide film and diminishes the formation of surface cracks and defects, which serve as primary sites for initial pitting formation and propagation. This also shows that the hatching distance is more influential than the scanning speed, showing that a reduced number of longer thermal cycles produces less thermal stresses and defects then multiple shorter thermal cycles [36]. The SEM images (Fig. 7) reveal disparities between samples 2 and 5, with S2 exhibiting fewer and smaller initial defects compared to S5, which employs a hatching distance of 1 µm. The presence of surface defects at higher areal energies has been documented in previous literature [37]. These defects intensify chloride attack and heighten the reactivity of the anions. Mechanical stresses at weak sites or flaws arising from electrostriction and surface tension effects may precipitate local breakdown events. In chloride-containing solutions, the hindrance to repassivation by chloride diminishes the likelihood of such breakdowns healing allowing for permanent pitting to be form [30].

Furthermore, samples 1, 4, and 5 possess a transpassivation zone where there is a sharp decrease in the anodic current density once the pitting resistance is surpassed. This phenomenon is attributed to the formation of a thicker oxide film with a lower chromium ion concentration, rendering further attacks more facile. However, samples 2 and 3 exhibit no such transpassive zone due to two reasons: first, the pitting resistance of their surfaces exceeds the transpassivation zone threshold of 0.4 V vs Ag/AgCl, and second, their favourable chromium oxide composition, primarily comprising Cr (III), enhances resistance to transpassivation [28]. This further shows the favourable long-term corrosion resistance of the optimized laser processed samples.

Based on the XPS depth profile analysis, it is evident that in S5, the laser processing has effectively removed the oxide layer due to the removal of the chromium enriched outer layer. This consistent composition observed throughout the entire depth profile indicates the absence of a passive layer, which explains the nearly non-existent passive behaviour observed in this sample, leading to immediate pitting breakdown. The uniform oxide layer produced can be attributed to the extended duration of exposure to the laser source. This prolonged exposure provides ample time for elemental diffusion, enabling the complete suppression of the initially formed thin chromium oxide layer by the subsequently produced iron oxide layer. This phenomenon underscores the critical role of time in the laser processing method, allowing for the formation of a uniform oxide layer on the surface and taking away the removals the beneficial effects seen for the non equilibrium oxidation seen at shorter time scales. From the longer term EIS it is evident that change in the RP value is more pronounced in S5 compared to S2, indicating that S5 experiences more significant passivation upon immersion in the solution, whereas S2, being prepassivated, undergoes a lesser increase in oxide layer growth.

The observed pitting morphology closely corresponds to the outcomes of the corrosion tests, indicating superior performance of S2 compared to S5 and the blank. S2 exhibits minimal pitting, primarily showcasing general corrosion, whereas the unprocessed samples and S5 display a higher quantity of larger pits, along with instances of oxide layer removal and delamination in S5. The heightened susceptibility to pitting in S5 can be attributed to the presence of cracks and pores in the

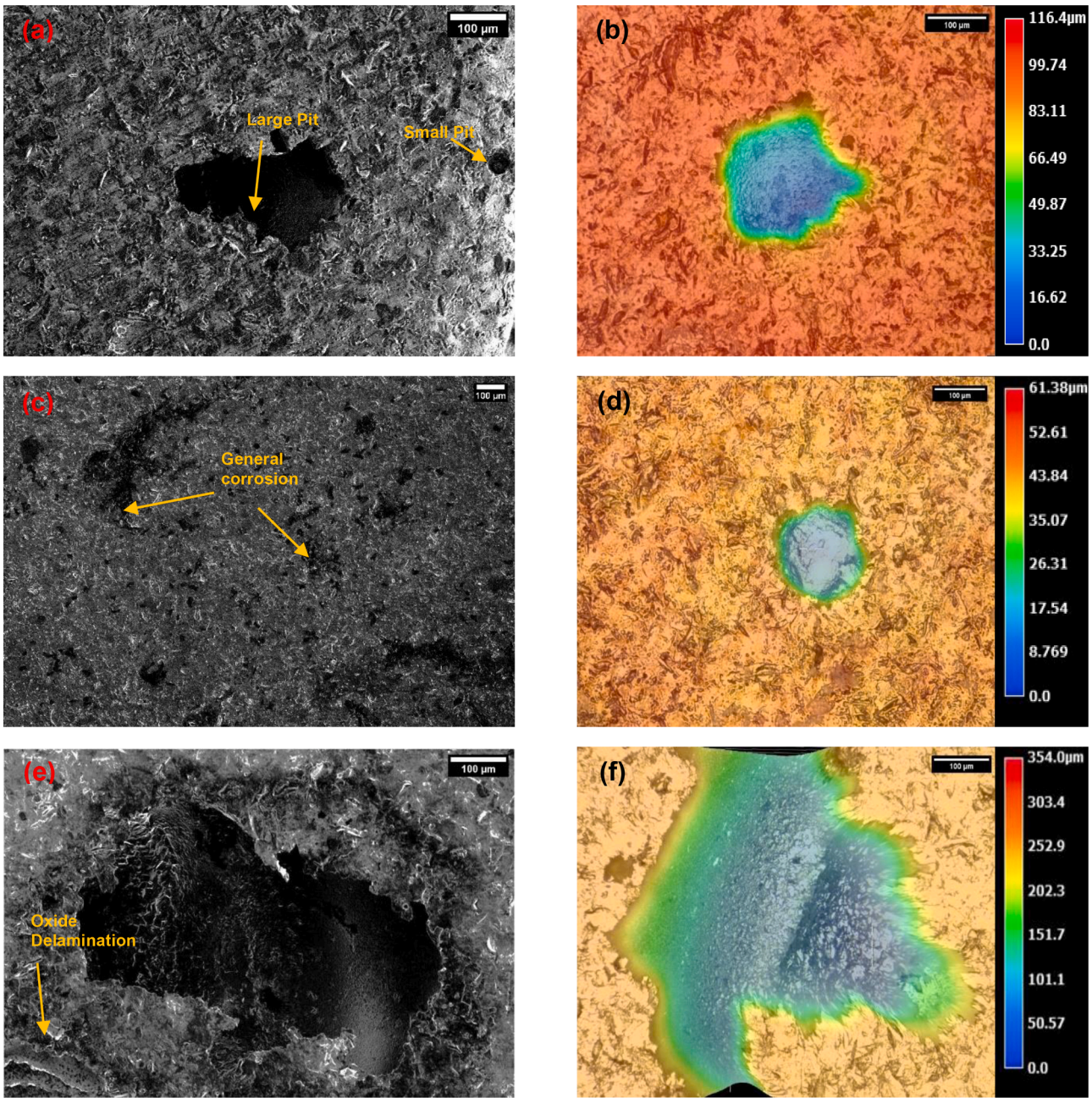

Fig. 8. (a) SEM image of unprocessed showing corrosion morphology, (b) optical profilometer of unprocessed pitting corrosion, (c) SEM image of S2 showing corrosion morphology,(d) optical profilometer of S2 pitting corrosion (e) SEM image of sample of S5, and (f) optical profilometer of S2 pitting corrosion.

oxide film post-processing, serving as initiation sites for pitting corrosion. Moreover, the Electrochemical Impedance Spectroscopy Equivalent Circuit (EIS EEC) employed to characterize the electrochemical behaviour supports this observation. The usage of a CPE+2 pore EEC for S5 indicates the presence of defects in the outer layer, consequently reducing the overall surface resistance. Conversely, SEM images of S2 reveal a smoother surface with evidence of surface remelting and solidification. The corresponding EEC of CPE + 2 suggests a more densely packed surface with fewer original defects. Further analysis of long-term EIS data highlights S2′s enhanced corrosion resistance compared to S5. S5′s Rp value sharply declines after day 5, accompanied by a change in EEC indicating the onset of pitting corrosion. In contrast, S2 exhibits a steady increase in resistance until day 2, maintaining this level throughout the 10-day test period without evident permanent surface breakdown.

Using the results from samples S2 and S3 specifically, it becomes evident how individual factors influence corrosion outcomes. Both samples share similar areal energies but differ in composition. S2 was produced with a high scan speed and low hatching distance, while S3 was prodices with a low scan speed and high hatching distance. These results highlight that hatching distance significantly affects pitting resistance due to its much lower impact on surface morphology. Conversely, lower areal energy plays a crucial role in corrosion currents, mainly influenced by the sensitive Cr/Fe ratio. S2, with slightly lower areal energy, demonstrated a 50 % increase in the Cr/Fe ratio compared to S3, illustrating the substantial impact of individual processing parameters. These results highlight for the first time the long term significant influence of laser processing parameters on the varying composition of elemental oxide layers on the surface and in the subsurface and in turn the corrosion performance of laser-processed SS316L

stainless steel.

5. Conclusion

The optimization of laser processing parameters for stainless steel corrosion resistance was conducted using two full factorial designs of experiments (DoE), focusing on laser power, scan speed, frequency, and hatching distance. This study has revealed several key fundamental insights on how the laser surface modification affects the surface chemistry and corrosion properties.

Areal energy Influence: Samples processed with reduced areal energy of under 3×10^{24} J/cm^2 demonstrated superior corrosion resistance that surpass that of unprocessed SS. Optimal parameters resulted in a peak pitting resistance of 509.15 mV and an Icorr value of 51.5 nA/cm^2, indicating significantly improved corrosion resistance compared to unprocessed samples, which resulted in a pitting resistance of 160.8 mV and an Icorr value of 502 nA/cm^2

Surface Composition Analysis: X-ray Photoelectron Spectroscopy (XPS) analysis highlighted the predominant presence of iron and chromium oxides on the surface with a Cr/Fe ratio exceeding 3.5 for the optimised sample (S3), resulting in significantly improved corrosion resistance where noticeable increases in corrosion current once the Cr/Fe ratio surpassed 1.0 with minimally changes in Icorr below 1.0. Depth profiling indicated variations in oxide layer composition and thickness, providing valuable insights into corrosion behaviour.

Surface Morphology: Scanning Electron Microscope (SEM) imaging confirmed the efficacy of laser processing in reducing surface defects and enhancing resistance to localized corrosion. Samples with optimized processing parameters exhibited smoother surfaces with fewer defects, contributing to improved corrosion resistance.

Corrosion Behaviour: Cyclic polarization tests demonstrated a clear correlation between surface composition, morphology, and corrosion resistance. Samples with higher chromium content and smoother surfaces exhibited superior resistance to localized corrosion.

Electrochemical Impedance Spectroscopy (EIS): EIS revealed higher resistance and lower capacitance in optimally processed samples, indicative of enhanced corrosion protection. The long-term impedance spectra provided valuable information on the evolution of the passive film over time showing either the building or breaking down of the passive film highlighting there stability under corrosive conditions.

Overall, the findings underscored the importance of areal energy, composition, and morphology in tailoring stainless steel surfaces for improved corrosion resistance through laser processing. These results provide valuable insights for the development of corrosion-resistant materials and surface engineering techniques in various industrial applications. Further research could explore additional factors influencing corrosion behaviour such as other laser processing parameters, metal compositions and environmental conditions for specific applications.

Funding

This publication has emanated from research supported by a research grant from Science Foundation Ireland (SFI) under Grant numbers 18/EPSRC-CDT/3584, 16/RC/3872 and is co-funded under the European Regional Development Fund and EPSRC (EP/R008841/1).

CRediT authorship contribution statement

Mark Swayne: Writing – review & editing, Writing – original draft, Visualization, Validation, Resources, Methodology, Investigation, Formal analysis, Data curation, Conceptualization. **Gopinath Perumal:** Writing – review & editing, Writing – original draft, Resources, Formal analysis, Data curation. **Dilli Babu Padmanaban:** Writing – review & editing, Resources, Data curation. **Davide Mariotti:** Writing – review & editing, Supervision, Software, Resources. **Dermot Brabazon:** Writing – review & editing, Writing – original draft, Supervision, Funding acquisition, Formal analysis, Conceptualization.

Declaration of competing interest

The authors declare the following financial interests/personal relationships which may be considered as potential competing interests: Mark Swayne reports financial support was provided by Dublin City University. If there are other authors, they declare that they have no known competing financial interests or personal relationships that could have appeared to influence the work reported in this paper.

Data Availability

Data will be made available on request.

Acknowledgements

This work is supported by I-Form, the Science Foundation Ireland Research Centre for Advanced Manufacturing. This work is also supported by Advanced Metallic Systems Centre of Doctorial Training (AMSCDT), which incorporates four universities namely Dublin City University (DCU), University College Dublin, The University of Sheffield and The University of Manchester. This work is in partnership PRO Stainless Design Ltd, a company based in Ireland. Science Foundation Ireland (18/EPSRC-CDT/3584) and the Engineering and Physical Sciences Research Council (EP/S022635/1) supported this work.

Supplementary materials

Supplementary material associated with this article can be found, in the online version, at doi:10.1016/j.apsadv.2024.100622.

References

[1] F.S. Shieu, M.J. Deng, S.H. Lin, Microstructure and corrosion resistance of a type 316L stainless steel, Corros. Sci. 40 (1998) 1267–1279, https://doi.org/10.1016/S0010-938X(97)00143-1.
[2] M. Obeidi, E. Mccarthy, S. Ubani, I. Ahad, D. Brabazon, Effect of surface roughness on CO2 laser absorption by 316L stainless steel and aluminum, Mater. Perform. Charact. 8 (2019) 20180091, https://doi.org/10.1520/MPC20180091.
[3] W. Pacquentin, N. Caron, R. Oltra, Nanosecond laser surface modification of AISI 304L stainless steel: influence the beam overlap on pitting corrosion resistance, Appl. Surf. Sci. 288 (2014) 34–39, https://doi.org/10.1016/j.apsusc.2013.09.086.
[4] E. Chikarakara, S. Naher, D. Brabazon, Spinodal decomposition in AISI 316L stainless steel via high-speed laser remelting, Appl. Surf. Sci. 302 (2014) 318–321, https://doi.org/10.1016/j.apsusc.2013.10.099.
[5] E.R.I. Mahmoud, S.Z. Khan, M. Ejaz, Laser surface cladding of mild steel with 316L stainless steel for anti-corrosion applications, Mater. Today Proc. 39 (2021) 1029–1033, https://doi.org/10.1016/j.matpr.2020.04.763.
[6] A. Dudek, B. Lisiecka, N. Radek, Ł.J. Orman, J. Pietraszek, Laser surface alloying of sintered stainless steel, Materials 15 (2022), https://doi.org/10.3390/ma15176061.
[7] J.D. Majumdar, A. Kumar, S. Pityana, I. Manna, Laser Surface melting of AISI 316L stainless steel for bio-implant application, Proc. Natl. Acad. Sci. India Sect. A 88 (2018) 387–403, https://doi.org/10.1007/s40010-018-0524-4.
[8] C.Y. Cui, X.G. Cui, X.D. Ren, M.J. Qi, J.D. Hu, Y.M. Wang, Surface oxidation phenomenon and mechanism of AISI 304 stainless steel induced by Nd:YAG pulsed laser, Appl. Surf. Sci. 305 (2014) 817–824, https://doi.org/10.1016/j.apsusc.2014.04.025.
[9] K. Kiasaleh, Gaussian beam characterization for laser beam propagation through translucent, multi-layer medium with random indices of refraction, in: 2015 IEEE Int. Conf. Sp. Opt. Syst. Appl., 2015, pp. 1–6, https://doi.org/10.1109/ICSOS.2015.7425082.
[10] Z.L. Li, H.Y. Zheng, K.M. Teh, Y.C. Liu, G.C. Lim, H.L. Seng, N.L. Yakovlev, Analysis of oxide formation induced by UV laser coloration of stainless steel, Appl. Surf. Sci. 256 (2009) 1582–1588, https://doi.org/10.1016/j.apsusc.2009.09.025.
[11] Y. Lu, X. Shi, Z. Huang, T. Li, M. Zhang, J. Czajkowski, T. Fabritius, M. Huttula, W. Cao, Nanosecond laser coloration on stainless steel surface, Sci. Rep. 7 (2017) 7092, https://doi.org/10.1038/s41598-017-07373-8.
[12] K.M. Łęcka, A.J. Antończak, B. Szubzda, M.R. Wójcik, B.D. Stępak, P. Szymczyk, M. Trzciński, M. Ozimek, K.M. Abramski, Effects of laser-induced oxidation on the corrosion resistance of AISI 304 stainless steel, J. Laser Appl. 28 (2016) 32009, https://doi.org/10.2351/1.4948726.

[13] P. Marcus, On some fundamental factors in the effect of alloying elements on passivation of alloys, Corros. Sci. 36 (1994) 2155–2158, https://doi.org/10.1016/0010-938X(94)90013-2.
[14] Q. Zhu, W. Sun, Y. Yoo, X. Zhang, N. Hunter, A. Mao, N. Li, X. Huang, P. Fan, X. Wang, B. Cui, Y. Lu, Enhance corrosion resistance of 304 stainless steel using nanosecond pulsed laser surface processing, Surf. Interfaces 42 (2023) 103479, https://doi.org/10.1016/j.surfin.2023.103479.
[15] T. Jwad, S. Deng, H. Butt, S. Dimov, Laser induced single spot oxidation of titanium, Appl. Surf. Sci. 387 (2016) 617–624, https://doi.org/10.1016/j.apsusc.2016.06.136.
[16] S.K. Lawrence, D.P. Adams, D.F. Bahr, N.R. Moody, Environmental resistance of oxide tags fabricated on 304L stainless steel via nanosecond pulsed laser irradiation, Surf. Coatings Technol. 285 (2016) 87–97, https://doi.org/10.1016/j.surfcoat.2015.11.021.
[17] R.K. Wild, Ion sputter rates of Cr—Mn—Fe spinel oxides, Surf. Interface Anal. 14 (1989) 239–244, https://doi.org/10.1002/sia.740140505.
[18] M.P. Seah, D. David, J.A. Davies, T.E. Jackman, C. Jeynes, C. Ortega, P.M. Read, C. J. Sofield, G. Weber, An intercomparison of absolute measurements of the oxygen and tantalum thickness of tantalum pentoxide reference materials, BCR 261, by six laboratories, Nucl. Instrum. Methods Phys. Res. Sect. B 30 (1988) 140–151, https://doi.org/10.1016/0168-583X(88)90110-3.
[19] Q. Yang, J.L. Luo, Effects of hydrogen on disorder of passive films and pitting susceptibility of type 310 stainless steel, J. Electrochem. Soc. 148 (2001) B29, https://doi.org/10.1149/1.1344529.
[20] T. Hanawa, S. Hiromoto, A. Yamamoto, D. Kuroda, K. Asami, XPS characterization of the surface oxide film of 316L stainless steel samples that were located in quasi-biological environments, Mater. Trans. 43 (2002) 3088–3092, https://doi.org/10.2320/matertrans.43.3088.
[21] J.-G. Choi, L.T. Thompson, XPS study of as-prepared and reduced molybdenum oxides, Appl. Surf. Sci. 93 (1996) 143–149, https://doi.org/10.1016/0169-4332(95)00317-7.
[22] R.-H. Jung, H. Tsuchiya, S. Fujimoto, XPS characterization of passive films formed on Type 304 stainless steel in humid atmosphere, Corros. Sci. 58 (2012) 62–68, https://doi.org/10.1016/j.corsci.2012.01.006.
[23] Y. Gui, X.B. Meng, Z.J. Zheng, Y. Gao, Critical temperature determination of detectable Cr diffusion enhancement by nanostructure through structural evolution analysis of the oxide films at 25–450°C on 304 stainless steel, Appl. Surf. Sci. 419 (2017) 512–521, https://doi.org/10.1016/j.apsusc.2017.04.133.
[24] R. Kirchheim, Growth kinetics of passive films, Electrochim. Acta. 32 (1987) 1619–1629, https://doi.org/10.1016/0013-4686(87)90015-6.
[25] R. Ovarfort, Critical pitting temperature measurements of stainless steels with an improved electrochemical method, Corros. Sci. 29 (1989) 987–993, https://doi.org/10.1016/0010-938X(89)90088-7.
[26] G.S. Frankel, Pitting corrosion of metals: a review of the critical factors, J. Electrochem. Soc. 145 (1998) 2186, https://doi.org/10.1149/1.1838615.
[27] R.C. Newman, 2001 W.R. Whitney award lecture: understanding the corrosion of stainless steel, Corrosion 57 (2001) 1030–1041, https://doi.org/10.5006/1.3281676.
[28] G. Song, Transpassivation of Fe–Cr–Ni stainless steels, Corros. Sci. 47 (2005) 1953–1987, https://doi.org/10.1016/j.corsci.2004.09.007.
[29] R.A. Buchanan, E.E. Stansbury, 4 - Electrochemical corrosion, in: S.E. Kutz (Ed.), Handbook of Environmental Degradation of Materials (Second Edition), William Andrew Publishing, Oxford, 2012, pp. 87–125, https://doi.org/10.1016/B978-1-4377-3455-3.00004-3.
[30] K. Darowicki, S. Krakowiak, P. Ślepski, Evaluation of pitting corrosion by means of dynamic electrochemical impedance spectroscopy, Electrochim. Acta 49 (2004) 2909–2918, https://doi.org/10.1016/j.electacta.2004.01.070.
[31] C.-O.A. Olsson, The influence of nitrogen and molybdenum on passive films formed on the austenoferritic stainless steel 2205 studied by AES and XPS, Corros. Sci. 37 (1995) 467–479, https://doi.org/10.1016/0010-938X(94)00148-Y.
[32] I. Olefjord, L. Wegrelius, Surface analysis of passive state, Corros. Sci. 31 (1990) 89–98, https://doi.org/10.1016/0010-938X(90)90095-M.
[33] E. De Vito, P. Marcus, XPS study of passive films formed on molybdenum-implanted austenitic stainless steels, Surf. Interface Anal. 19 (1992) 403–408, https://doi.org/10.1002/sia.740190175.
[34] M. Tsuchiya, S.K.R.S. Sankaranarayanan, S. Ramanathan, Photon-assisted oxidation and oxide thin film synthesis: a review, Prog. Mater. Sci. 54 (2009) 981–1057, https://doi.org/10.1016/j.pmatsci.2009.04.003.
[35] L. Nánai, R. Vajtai, I. Kovács, I. Hevesi, On the kinetics of laser-light-induced oxidation constants of vanadium, J. Less Common Met. 152 (1989) L23–L26, https://doi.org/10.1016/0022-5088(89)90104-5.
[36] M.C.C. Monu, Y. Afkham, J.C. Chekotu, E.J. Ekoi, H. Gu, C. Teng, J. Ginn, J. Gaughran, D. Brabazon, Bi-directional scan pattern effects on residual stresses and distortion in as-built nitinol parts: a trend analysis simulation study, Integr. Mater. Manuf. Innov. 12 (2023) 52–69, https://doi.org/10.1007/s40192-023-00292-9.
[37] B. Szubzda, A. Antończak, P. Kozioł, Ł. Łazarek, B. Stępak, K. Łęcka, A. Szmaja, M. Ozimek, Corrosion resistance of the AISI 304, 316 and 321 stainless steel surfaces modified by laser, IOP Conf. Ser. Mater. Sci. Eng. 113 (2016) 12017, https://doi.org/10.1088/1757-899X/113/1/012017.